Role of atmosphere-ocean interactions in supermodeling the tropical Pacific climate

Mao-Lin Shen, Noel Keenlyside, Bhuwan C. Bhatt, and Gregory S. Duane

Citation: Chaos **27**, 126704 (2017);
View online: https://doi.org/10.1063/1.4990713
View Table of Contents: http://aip.scitation.org/toc/cha/27/12
Published by the American Institute of Physics

Role of atmosphere-ocean interactions in supermodeling the tropical Pacific climate

Mao-Lin Shen,[1] Noel Keenlyside,[1] Bhuwan C. Bhatt,[1] and Gregory S. Duane[1,2]
[1]*Geophysical Institute, University of Bergen and Bjerknes Centre for Climate Research, Bergen 5007, Norway*
[2]*University of Colorado Boulder, Boulder, Colorado 80309-0311, USA*

(Received 16 June 2017; accepted 5 December 2017; published online 29 December 2017)

The supermodel strategy interactively combines several models to outperform the individual models comprising it. A key advantage of the approach is that nonlinear improvements can be achieved, in contrast to the linear weighted combination of individual unconnected models. This property is found in a climate supermodel constructed by coupling two versions of an atmospheric model differing only in their convection scheme to a single ocean model. The ocean model receives a weighted combination of the momentum and heat fluxes. Optimal weights can produce a supermodel with a basic state similar to observations: a single Intertropical Convergence zone (ITCZ), with a western Pacific warm pool and an equatorial cold tongue. This is in stark contrast to the erroneous double ITCZ pattern simulated by both of the two stand-alone coupled models. By varying weights, we develop a conceptual scheme to explain how combining the momentum fluxes of the two different atmospheric models affects equatorial upwelling and surface wind feedback so as to give a realistic basic state in the tropical Pacific. In particular, we propose a mechanism based on the competing influences of equatorial zonal wind and off-equatorial wind stress curl in driving equatorial upwelling in the coupled models. Our results show how nonlinear ocean-atmosphere interaction is essential in combining these two effects to build different sea surface temperature structures, some of which are realistic. They also provide some insight into observed and modelled tropical Pacific climate. *Published by AIP Publishing.*
https://doi.org/10.1063/1.4990713

Predicting the behavior of a nonlinear dynamical system is particularly challenging when model imperfections cause a misrepresentation of the system's attractor. A good example is the limitation of climate prediction by large model systematic error. Supermodeling is a recently proposed approach in which multiple models are combined interactively to reduce model error and improve prediction. Synchronization of the different models allows nonlinear improvements in the representation of the dynamical system, making the approach superior to the standard linear weighted combination of ouputs of the individual unconnected models. Here we interconnect two different versions of a climate model to achieve a nonlinear improvement in the representation of tropical Pacific climate. Three structurally different model states can be simulated by changing the strength of the model connection coefficients: an equatorially symmetric pattern in which the upper ocean is cooler at the equator and warmer off the equator (a typical erroneous state of current climate models), the reverse pattern (a state associated with the warming of the central and eastern tropical Pacific), and an equatorially asymmetric pattern in which the upper ocean is warmer in the Northern Hemisphere (NH) (a realistic basic state in the tropical Pacific). A conceptual analysis can explain the different phases in terms of atmosphere-ocean interactions involving wind stress patterns in the equatorial and off-equatorial regions. Non-linear interactions inherent to the tropical Pacific climate can explain how the effects can combine to produce the supermodel (SUMO) state. Thus, we provide a qualitative understanding of the mechanism for the success of the novel supermodeling approach.

I. INTRODUCTION

Numerical models of complex systems are imperfect because of their necessary simplifications. It has been long recognized that the combination of the outputs from imperfect models can lead to the cancellation of model errors and improved depiction of the statistics of the underlying system.[1] However, the linear combination of model outputs can lead to only a linear reduction of error, and nonlinear properties of the system cannot be improved.

Unpredictable systems can be synchronized when connected through few variables—so-called chaos synchronization, a well-known phenomenon in nonlinear dynamical systems.[2] It has been demonstrated in quasigeostrophic models[3–5] and in an atmosphere general circulation model (AGCM).[6] The so-called supermodeling approach[7] interactively combines multiple imperfect complex climate models and tends to synchronize model states. The synchronization of the different imperfect models through their interactive coupling allows them to shadow an underlying strange attractor. Errors in the individual models can thus be compensated dynamically, allowing the supermodel to better capture the nonlinear character of the system.

Another powerful advantage of a supermodel is that it is also a dynamical model and can be used in the same manner as any of the constituent models. For example, it can be used to forecast future behavior of the system, as in weather prediction. In contrast, the linear combination of a series of imperfect model forecasts is only useful for describing the nature state during the initial deterministic period; thereafter, only a statistical or probabilistic description is possible. While the goal for climate projection is not to predict future states as a function of time, as in weather prediction, it is thought that the development of climate supermodels will ultimately be useful for forecast models as well.

The conditions under which a supermodel can outperform the combined output of the separately run models comprising the supermodel are not well understood. Understanding these conditions is a challenge when dealing with a high-dimensional nonlinear systems.[8] Here we propose a mechanism to explain the supermodel results that is supported by perturbation analysis of the same physical effects in the linear regime. In particular, we investigate how the linear combination of fluxes in two climate models can lead to the nonlinear improvement in the simulation of the tropical Pacific that was recently shown.[9] Section II summarizes the relevant background of the tropical Pacific climate and the performance of climate models in simulating it. Section III introduces the supermodel used here to simulate the tropical Pacific. The "phases" of the supermodel solutions are investigated in Sec. IV, and the nonlinear properties of the supermodel configuration are explained in Sec. V with the aid of a conceptual analysis of the underlying physics. Section VI draws implications for the supermodeling approach generally.

II. TROPICAL PACIFIC CLIMATE AND ITS SIMULATION BY CLIMATE MODELS

The tropical Pacific climate has several key features (Fig. 1). The Intertropical Convergence Zone (ITCZ) is a band of precipitation situated north of the equator and extending from the western Pacific to Central America. The western Pacific is also a region of intense precipitation, with a zone of precipitation—the South Pacific Convergence Zone (SPCZ)—extending over the South Pacific islands.

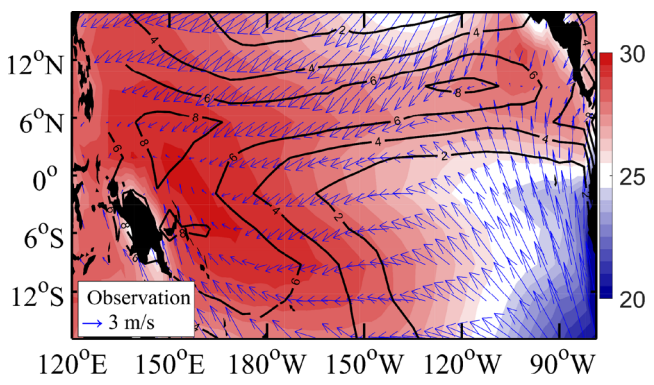

FIG. 1. Climatological mean state of SST (shading, °C) and precipitation (contour, mm/day) from HadISST[12] and GPCP (data retrieved from website http://www.esrl.noaa.gov/psd) observations, and 10 m winds (vectors) from the NCEP reanalysis.[11] The HadISST data were retrieved from the website http://www.metoffice.gov.uk/hadobs/hadisst.

There is also notable absence of precipitation in the south eastern equatorial Pacific. The region of warm water in the western Pacific is known as the western Pacific warm pool. The surface trade winds cause water to converge in the precipitation bands. The water vapor condenses in strong vertical motions associated with atmospheric convection and precipitates. The wind stress associated with the trade winds induces upwelling of cold water from below over the central and eastern equatorial Pacific, creating a feature known as the equatorial cold tongue. These features comprise a distinctive precipitation and sea surface temperature (SST) pattern that reflects a key nonlinear relationship between SST and precipitation, with intense precipitation occurrence only when SST is higher than 28 °C.[10]

The complex coupled ocean-atmosphere interactions explaining the tropical Pacific climatology (Fig. 1) are not fully understood. A question that continues to puzzle climate scientists is the non-existence of a continuous band of precipitation south of the equator, similar to the ITCZ north of the equator. Early studies attributed this to the configuration of the South and North American coastlines that favor stronger coastal upwelling in the Southern Hemisphere (SH) suppressing atmospheric convection[13] and that is reinforced by a low-level cloud SST feedback.[14] In addition, the large-scale tropical atmospheric east-west Walker Circulation (see Fig. 7 and description in Sect. IV B) that is driven by atmospheric convection over the western Pacific is associated with subsidence over the southeastern Pacific. The interplay between atmospheric convection occurring over warm SST and suppression of convection by large-scale subsidence[15] likely contributes to the north-south precipitation asymmetries.[16] The east-west temperature gradient in the South Pacific is a key factor.[17] Large-scale global energy budget considerations also contribute to a preference for a Northern Hemisphere (NH) ITCZ.[18,19]

Accurate simulation of the tropical Pacific climate is a long-standing challenge reflecting our incomplete understanding of the mechanisms. Systematic model errors in earlier generations of general circulation models (GCMs) were often characterized by permanent El Niño like conditions.[20] However, a double ITCZ, a too strong cold tongue, and too warm waters off the South American coast are more common and persistent problems[21] that appear in current GCMs.[22,23] The cause of the double ITCZ bias has been attributed to inaccurate representation of convective processes in the tropics,[16] misrepresentation of low-level cloud-SST feedbacks,[24] and errors in the SH extra-tropical radiation budget.[25,26] Whereas the double ITCZ error is simulated even by atmospheric GCM's with prescribed observed SST fields,[27] the excessive trade winds associated with the equatorial cold tongue bias appear to be associated with the Bjerknes feedback[28] between atmosphere and ocean.

The Bjerknes feedback is a positive feedback that amplifies El Niño and La Niña events in the tropical Pacific.[29] El Niño events are associated with the warming of the central and eastern tropical Pacific, while La Niña events are the reverse, with a sustained cooling of these same areas. During El Niño, warm surface waters in the eastern Pacific drive an east- and equator-ward shift in atmospheric convection and a

weakening of the easterly trade winds, which in turn enhances the warming. The Bjerknes feedback leads to a rapid warming in the east and strong reduction in the east-west equatorial SST gradient. The feedback operates in a similar manner for negative anomalies. A second key process is the exchange of heat from the tropics to the subtropics that is regulated by the tropical-subtropical cells—a meridional overturning circulation in the upper few hundred meters of the ocean that extends from the equatorial region into the subtropics.[30,31] This circulation consists of two components that are both driven by the easterly surface trade winds: (1) the subtropical cells are driven by the east-west component of the trade winds that causes surface waters to move poleward due to the Coriolis effect, sink in the subtropics, and then return to the equator where they are upwelled back to the surface.[32,33] (2) The tropical cells are driven by the gradients in the trade winds which cause downwelling of water around 5–10°S and 5–10°N and upwelling of water at the equator[34,35] as shown in Fig. 2. The recharge and discharge of heat by this circulation provides the delayed negative feedback leading to the decay of El Niño and La Niña events.[29] The strength of these cells and the temperature contrast between the tropics and subtropics are of key importance in explaining the strength of the equatorial cold tongue.[36,37]

III. SUPERMODEL OF THE TROPICAL PACIFIC

The supermodel (SUMO) that we recently developed demonstrated the potential to mitigate the double ITCZ behavior found in its constituent climate models (Fig. 2, Ref. 9). SUMO extends the interactive ensemble approach. In the standard interactive ensemble, multiple identical atmospheric models are coupled to a single ocean model. The ocean model receives the average of atmospheric surface fluxes of heat, momentum, and mass, while each atmospheric model receives the SST from the ocean model.[38] SUMO extends the standard interactive ensemble to couple two different atmospheric models to a single ocean model, but in contrast to the earlier study,[39] the atmospheric fluxes from the two different models are optimally weighted to simulate an improved tropical Pacific climate. The feedbacks summarized in Sec. II induce approximate synchronization between the two atmospheric models over the tropical Pacific.

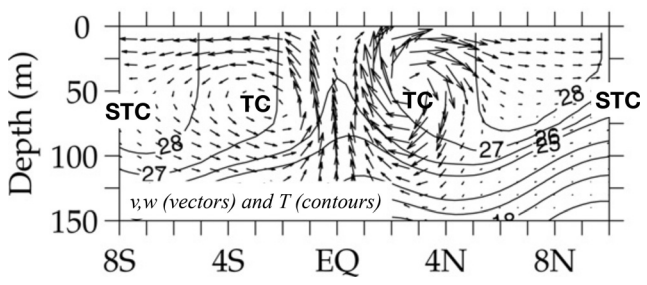

FIG. 2. Modelled tropical (TC) and subtropical cells (STC) along 140°W with vectors denoting the vertical and meridional velocity and contours the water temperature T. The strong gradient in T marks the thermocline, separating the warm surface and cold subsurface waters. Note the strong upwelling of cold water at the equator and the downwelling around 5–10°S and 5–10°N. Adapted from Fig. 1(g) in Ref. 34.

The constituents of SUMO are based on the Community Earth System Models (COSMOS) developed at Max-Planck-Institut für Meteorologie, Germany.[40] The atmospheric general circulation model (AGCM) of COSMOS is the 5th generation European Centre Hamburg general circulation model (ECHAM5),[41] and oceanic GCM is Max Planck Institute Ocean Model (MPIOM).[42] The atmosphere and ocean components are coupled by the coupler OASIS3[43] (Ocean Atmosphere Sea Ice Soil). The AGCMs employ T31 spectral resolution (i.e., ∼3.75°) and 19 vertical levels, and the ocean employs a rotated curvilinear grid with an approximate 3° horizontal resolution and 40 vertical levels. We use two versions of the COSMOS model that differ only in the cumulus parameterization scheme: COSMOS-N uses the Nordeng[44] scheme and COSMOS-T uses the Tiedtke[45] scheme. Although both schemes favor convection in regions with maximum boundary layer moist static energy,[46] in COSMOS they produce different climatologies over the tropical Pacific Ocean and both have substantial errors, which are similar in structure to those of many current climate models (Fig. 3).

SUMO is constructed by coupling the two versions of ECHAM5 to a single MPIOM version: Both atmosphere models calculate the air-sea fluxes based on the same SST and the ocean receives a weighted average of the air-sea fluxes. A different combination of weights is used for each of the air-sea fluxes felt by the common ocean—heat, momentum, and freshwater. The sum of the weights over the two AGCMs equals unity, for each type of air-sea flux, so as to maintain conservation globally. We label the weights for the AGCM with the Nordeng convection scheme, α, β, and γ of heat flux, momentum flux, and freshwater, respectively.

That is, let the two COSMOS models be given by

$$\dot{\boldsymbol{A}} = f_N(\boldsymbol{A}, \boldsymbol{Q}_N(\boldsymbol{A},\boldsymbol{O}),\, \boldsymbol{\tau}_N(\boldsymbol{A},\boldsymbol{O}), \boldsymbol{q}_N(\boldsymbol{A},\boldsymbol{O})), \tag{1a}$$

$$\dot{\boldsymbol{O}} = g(\boldsymbol{O}, \boldsymbol{Q}_N(\boldsymbol{A},\boldsymbol{O}),\, \boldsymbol{\tau}_N(\boldsymbol{A},\boldsymbol{O}), \boldsymbol{q}_N(\boldsymbol{A},\boldsymbol{O})), \tag{1b}$$

and

$$\dot{\boldsymbol{A}} = f_T(\boldsymbol{A}, \boldsymbol{Q}_T(\boldsymbol{A},\boldsymbol{O}),\, \boldsymbol{\tau}_T(\boldsymbol{A},\boldsymbol{O}), \boldsymbol{q}_T(\boldsymbol{A},\boldsymbol{O})), \tag{2a}$$

$$\dot{\boldsymbol{O}} = g(\boldsymbol{O}, \boldsymbol{Q}_T(\boldsymbol{A},\boldsymbol{O}),\, \boldsymbol{\tau}_T(\boldsymbol{A},\boldsymbol{O}), \boldsymbol{q}_T(\boldsymbol{A},\boldsymbol{O})), \tag{2b}$$

where f_N and f_T are the dynamics describing the evolution of the atmospheric state vector $\boldsymbol{A}$ in the Nordeng and Tiedtke models, respectively, which involves a dependence on the atmosphere-ocean fluxes $\boldsymbol{Q}$, $\boldsymbol{\tau}$, and $\boldsymbol{q}$, which depend on the states of atmosphere and ocean in a different way for each model, denoted by the different subscripts. Here $\boldsymbol{Q}$ is the heat flux (between atmosphere and ocean), $\boldsymbol{\tau}$ the momentum flux (due to surface wind stress), and $\boldsymbol{q}$ water flux (precipitation minus evaporation). The ocean state $\boldsymbol{O}$ evolves according to the dynamics g which is the same in both models. The supermodel state is defined by conjoining three state vectors $\boldsymbol{A_N}$, $\boldsymbol{A_T}$, and $\boldsymbol{O}$. The state evolves according to

$$\dot{\boldsymbol{A}}_N = f_N(\boldsymbol{A}_N, \boldsymbol{Q}_N(\boldsymbol{A}_N,\boldsymbol{O}),\, \boldsymbol{\tau}_N(\boldsymbol{A}_N,\boldsymbol{O}), \boldsymbol{q}_N(\boldsymbol{A}_N,\boldsymbol{O})), \tag{3a}$$

$$\dot{\boldsymbol{A}}_T = f_T(\boldsymbol{A}_T, \boldsymbol{Q}_T(\boldsymbol{A}_T,\boldsymbol{O}),\, \boldsymbol{\tau}_T(\boldsymbol{A}_T,\boldsymbol{O}), \boldsymbol{q}_T(\boldsymbol{A}_T,\boldsymbol{O})), \tag{3b}$$

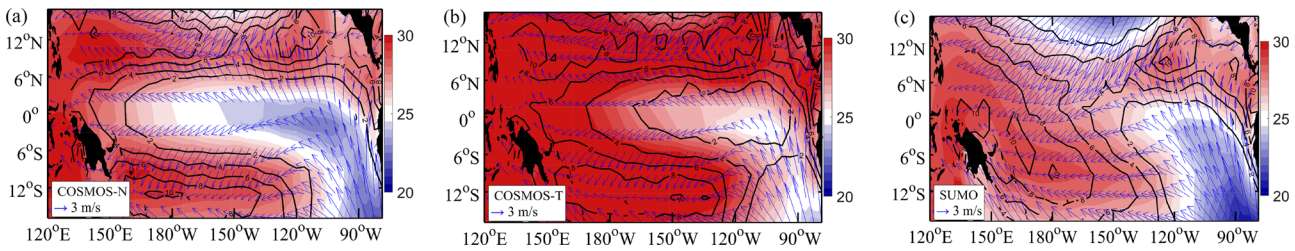

FIG. 3. Climatological mean states of SST (shading, °C), precipitation (contour, mm/day), and 10 m winds (vectors) for COSMOS-N (left panel), COSMOS-T (center panel), and SUMO (right panel).

$$\dot{\boldsymbol{O}} = g(\boldsymbol{O}, \alpha \boldsymbol{Q}_N(\boldsymbol{A}_N, \boldsymbol{O}) + (1-\alpha)\boldsymbol{Q}_T(\boldsymbol{A}_T, \boldsymbol{O}), \beta \boldsymbol{\tau}_N(\boldsymbol{A}_N, \boldsymbol{O}) + (1-\beta)\boldsymbol{\tau}_T(\boldsymbol{A}_T, \boldsymbol{O}), \gamma \boldsymbol{q}_N(\boldsymbol{A}_N, \boldsymbol{O}) + (1-\gamma)\boldsymbol{q}_T(\boldsymbol{A}_T, \boldsymbol{O})). \quad (3c)$$

The weights are free parameters that are optimized so that the 30 year mean simulated climatology of SST over the tropical Pacific region is closest to the observed climatology. A performance index[1] is defined as the root of the area-averaged squared difference between the observed and simulated SST climatology in the region bounded by (160°E-90°W, 10°S-10°N). The Nelder-Meade[47] machine learning algorithm is used to iteratively find weights that correspond to the smallest value of the performance index. The Nelder-Meade algorithm accomplishes gradient descent in the performance index without computing a gradient, by considering simplices of nearby test points in weight space. A total of 300 performance index evaluations were executed for different combinations of the weights (α, β, γ). The optimal values correspond to $(\alpha_o, \beta_o, \gamma_o) = (1.210, 0.423, 0.682)$. The supermodel with these optimal weights is referred to as SUMO, and the subscript o indicates that a term is from SUMO. Both the SST climatology over the tropical Pacific (Fig. 3) and the El Niño Southern Oscillation (ENSO) dynamics are much improved compared to the COSMOS-N and COSMOS-T models.[9]

IV. NON-LINEAR BEHAVIOR OF THE SUPERMODEL

The constituent models COSMOS-T and COSMOS-N exhibit rather similar SST patterns, while the SUMO SST pattern is quite different and cannot be understood as a linear combination of two constituent model states (Fig. 3). The same holds for the precipitation patterns as expected since they are closely related to the underlying SST. Therefore, to understand how the interactively combined system is able to produce a pattern that is structurally different from the constituent models, we construct a phase diagram in weight space characterizing the solutions, considering only SST.

A. Phases of the supermodel

The phase diagram is estimated from 450 simulations with interactive ensemble models differing in their weights; these include those performed to train the supermodel. The training showed that the water flux weights do not have a large influence on the structure of the SST climatology. Therefore the structure and error of the SST climatology is considered as a function of the heat and momentum flux weights only. The phase diagram is constructed by first plotting the performance index (noted by colors) for all the intermediate models as function of the heat flux weight (α, ordinate) and momentum flux weight (β, abscissa). The distribution shows a region of smaller (better) performance indices around $\alpha = 0.7 - 1.3$ and $\beta = 0.4 - 0.6$ where the SUMO model is located $(\alpha_o = 1.210, \beta_o = 0.423)$. Although most of the intermediate models clearly show larger tropical biases as well as structurally different SST patterns compared to observations, they provide insight into the physical cause of the transition from one type of climatological SST pattern into another.

Three structurally different possible model states are identified by varying the weights and are subjectively characterized: A classical double ITCZ found in COSMOS-T (but simulated also by COSMOS-N), a single ITCZ simulated by SUMO, and El Niño case (Fig. 4). The El Niño exhibits no cold tongue with warm SST and precipitation extending across the equatorial Pacific and with weak surface trade winds. By correlating the simulated tropical SST patterns with these three selected cases, we roughly identify the different regions of the phase diagram that they occupy (separated by black dashed lines in Fig. 5, where there is no strong correlation with any one case). A fourth region of the phase diagram encompassing the COSMOS-N is denoted as uncertain because no simulations were performed for these weights. While the phase boundaries are not exact, they indicate the qualitative change in the SST structure or phases due to the change in heat and momentum flux weights. The phase diagram indicates that structural SST changes are primarily due to changes in the momentum flux weight.

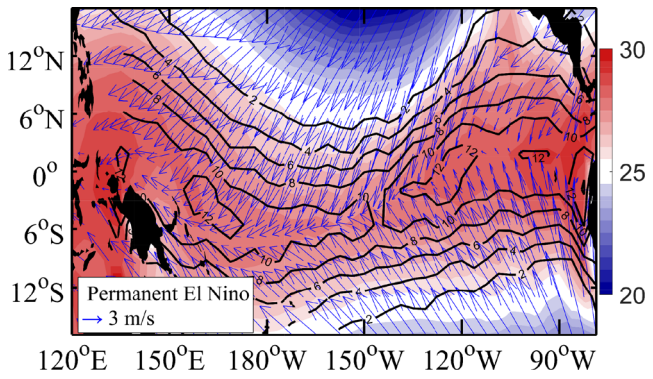

FIG. 4. As in Fig. 3, but for the El Niño like case with the following weights $(\alpha, \beta, \gamma) = (1.210, 0.923, 0.682)$.

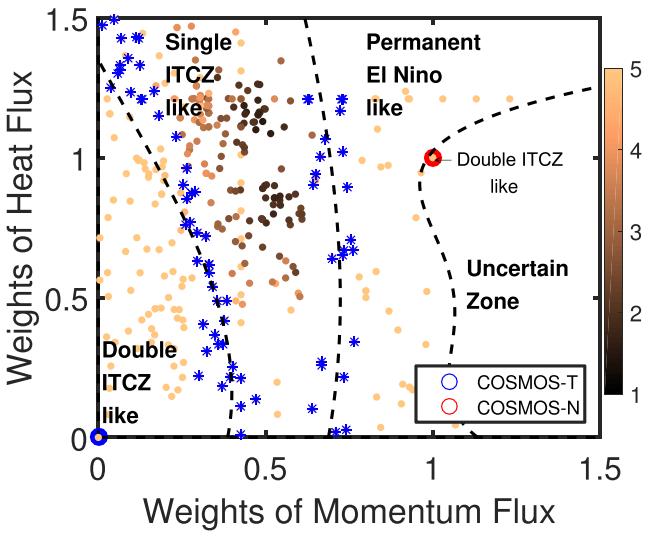

FIG. 5. Phase diagram showing the error in the SST climatology of the supermodel as a function of heat flux and momentum weights (colored dots—darker color, for lower index, indicates better performance). Three canonical SST patterns are distinguished (double ITCZ, single ITCZ, and El Niño) and regions are defined that contain SST climatologies with high pattern correlations with one of these canonical patterns. The region boundaries correspond to SST climatologies (blue asterisks) not resembling any of these three canonical patterns (pattern correlations lower than 0.92) and can be regarded as phase boundaries. Four regions (double ITCZ, single ITCZ, El Niño and uncertain zone) are roughly divided by dashed lines.

B. Proposed mechanism for the non-monotonic dependence of the supermodel behavior on the weights of the constituent models

The supermodel exhibits the single ITCZ found in observations, while the COSMOS-N and COSMOS-T models distort the ITCZ in similar ways, with an excessive cold tongue in their mean states. How can the supermodel, with positive weighting coefficients, combine the similar errors of the two constituent models so as to remove those errors? Here we introduce a plausible mechanism for the non-monotonic behavior of the supermodel combination based on well-known theory regarding tropical ocean circulation and El Niño,[29,48] which involves coupled ocean-atmosphere feedbacks that amplify the intrinsically different response to the SST distribution of the Nordeng and Tiedtke atmospheres.

The strength and east-west extent of the equatorial cold tongue are determined by the upwelling of colder subsurface waters. As changes in the momentum flux dominate structural changes of the equatorial SST, we can assume that it is changes in the wind driven ocean circulation that determine the changes in the cold tongue strength and extent, rather than the temperature of the upwelled water.

The strength of the equatorial upwelling can be considered as resulting from two components: (1) upwelling at the equator driven by local winds and (2) upwelling at the equator driven by downwelling off the equator and in the subtropics. Together, the two effects merge in the tropical ocean cell that is part of the complex 3-dimensional TC-STC circulation (Fig. 2). We argue that the different regions in the phase diagram are due to intrinsic differences in the wind stress and precipitation response to SST changes in the Nordeng and Tiedtke atmosphere models and the subsequent influence of the wind stress response on both contributions to the equatorial upwelling.

The intrinsically different response of the Nordeng and Tietdkte atmosphere models to the distribution of SST is deduced from uncoupled simulations with both models forced by the same prescribed observed SST climatology. As aforementioned, the only difference between the two AGCMs is in the convection scheme, which influences vertical profiles of temperature and humidity and the spatial distribution of precipitation and wind through changes in convective activity.

Under observed climatological SST conditions, the Nordeng atmosphere model exhibits stronger easterly trade winds and enhanced equatorward winds in both the western equatorial north Pacific and in central equatorial south Pacific, as compared to the Tiedtke atmosphere model (Fig. 6). This is associated with greater precipitation simulated by the Nordeng atmosphere model over the western equatorial Pacific because the Nordeng convection scheme favors convection on the equatorward side of the ITCZ.[46]

The difference in wind response between Nordeng and Tiedtke is a manifestation of the tropical-Pacific-wide 3D atmospheric circulation (Fig. 7). The stronger easterlies at the equator are due to the stronger so-called Walker circulation with rising motions in the tropical west Pacific and sinking motions in the east. The stronger rising motions enhance the so-called Hadley circulation with sinking motions in the sub-tropics and stronger equator-ward trade winds at surface.

When the atmosphere models are coupled to an ocean model, the differences in the winds affect the upwelling of cold water in the cold tongue at the equator. Ekman theory links the wind stress at the surface to the vertical velocity at thermocline depth. On the basis of this theory, we will argue how the wind difference between Nordeng and Tiedtke might affect the upwelling of cold water at the equator. The focus

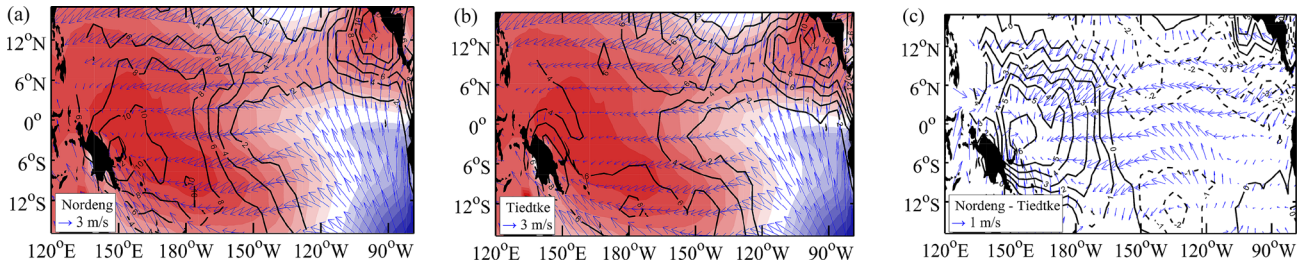

FIG. 6. AGCM simulations of Nordeng (left) and Tiedtke (middle) atmospheres with prescribed climatological mean state of SST (shading, same as Fig. 1 but in model resolution). Right panel shows the intrinsic difference of the two AGCMs. Precipitation (contour, mm/day) and 10 m winds (vectors) are superimposed.

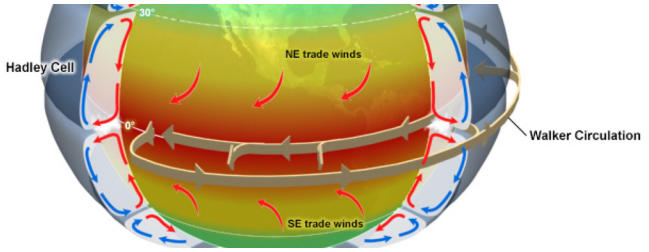

FIG. 7. Schematic showing the basic setup of the main global circulations and prevailing global winds including the three-dimensional structure of Walker circulation and Hadley Cell (by the COMET program, http://www.comet.ucar.edu/).

will be on the two most apparent differences: the stronger easterlies at the equator and the stronger equator-ward flow regions in Nordeng compared to Tiedtke.

In terms of such considerations, we attempt to explain in detail how the double ITCZ behavior could arise both for $\beta = 1$ and $\beta = 0$. The effect of changing the momentum flux weights towards pure Nordeng appears to come primarily through Ekman pumping associated with the greater easterly wind stress in the central and eastern Pacific (Fig. 6), and the difference is magnified by the Bjerknes feedback. The relevant equation is the ocean momentum equation

$$\frac{Du}{Dt} = -\frac{1}{\rho}\frac{\partial P}{\partial x} + \frac{1}{\rho}\frac{\partial \tau^x}{\partial z} + fv - \epsilon_s u, \tag{4a}$$

$$\frac{Dv}{Dt} = -\frac{1}{\rho}\frac{\partial P}{\partial y} + \frac{1}{\rho}\frac{\partial \tau^y}{\partial z} - fu - \epsilon_s v, \tag{4b}$$

where u, v, and w denote the east-west (zonal), north-south (meridional), and vertical velocities, respectively, and positive x, y, and z the corresponding eastward, northward, and upward directions. ρ is the density of the ocean water, P is the pressure, and τ^x and τ^y are the zonal and meridional Reynolds stress. $\frac{D}{Dt} \equiv \frac{\partial}{\partial t} + u\frac{\partial}{\partial x} + v\frac{\partial}{\partial y} + w\frac{\partial}{\partial z}$. At the sea surface $z = 0$, $\tau^x = \tau^{x0}$, $\tau^y = \tau^{y0}$ correspond to the surface wind stresses. $f = 2\Omega \sin\phi$ is the Coriolis parameter, with Ω the angular velocity of the Earth and ϕ the latitude. ϵ_s represents a linear friction. We first focus on the effect of zonal wind stress at the equator on the equatorial upwelling. We solve the steady-state linear momentum balance equation ($\frac{Du}{Dt} = 0$, $\frac{Dv}{Dt} = 0$), neglecting f in the zonal momentum budget (4a) and neglecting pressure gradients, finding $u = \frac{1}{\rho\epsilon_s}\frac{\partial \tau^x}{\partial z}$. Substituting in (4b), where we also neglect τ_y we find the Ekman balance $v = -\frac{f}{\rho{\epsilon_s}^2}\frac{\partial \tau^x}{\partial z}$.[48]

From mass conservation $\frac{\partial u}{\partial x} + \frac{\partial v}{\partial y} + \frac{\partial w}{\partial z} = 0$, where $\frac{\partial u}{\partial x}$ is negligible, we find

$$\frac{\partial w}{\partial z} = -\frac{\partial v}{\partial y} = -\frac{1}{\rho{\epsilon_s}^2}\frac{\partial f}{\partial y}\frac{\partial \tau^x}{\partial z}. \tag{5}$$

Assuming $w = 0$ at the surface, and integrating vertically downward to the thermocline, we find

$$-w^{\tau^x}_{y=0^o} \propto \frac{\partial f}{\partial y}\tau^x \tag{6}$$

at the thermocline. The upwelling velocity at this depth is important since the thermocline marks an abrupt temperature gradient between warm surface waters and cold subsurface waters. Since upwelling affects SST, the effect of increased easterly wind stress τ^x, which leads to increased equatorial upwelling $w^{\tau^x}_{y=0^o}$, is to lower the SST, extend the cold tongue, and split the ITCZ. The positive Bjerknes feedback amplifies the easterly wind stress and the associated cooling of SST at the equator. This explains the strong cold tongue in the Nordeng case and associated double ITCZ (Fig. 3 left panel, $\beta = 1$ case in the phase diagram Fig. 5).

While the explanation of the double ITCZ in Nordeng seems due to effects in the vertical equatorial plane, the effect of changing the momentum flux weights toward pure Tiedtke (i.e., $\beta \to 0$) appears to come from the full 3-dimensional structure of the atmospheric and oceanic circulations. So we next discuss the effect of the off-equatorial winds on the equatorial upwelling. Neglecting the linear friction leads to the Ekman balance for u and v: $u = \frac{1}{\rho f}\frac{\partial \tau^y}{\partial z}$, $v = -\frac{1}{\rho f}\frac{\partial \tau^x}{\partial z}$. Vertical motions will be induced if the horizontal Ekman currents converge or diverge since mass conservation implies $\frac{\partial w}{\partial z} = -\frac{\partial u}{\partial x} - \frac{\partial v}{\partial y}$. Integrating downward from the surface to the depth of the Ekman layer, D, gives $w_{z=0} - w_{z=-D} = \frac{1}{\rho f}\left(-\frac{\partial \tau^y}{\partial x} + \frac{\partial \tau^x}{\partial y}\right) = -\frac{1}{\rho f}\nabla \times \boldsymbol{\tau}$. w is zero at the sea surface ($w_{z=0} = 0$), and $\boldsymbol{\tau}$ decreases linearly from a value equal to wind stress at the sea surface to zero at depth D. Thus positive wind stress curl induces upwelling at the depth of the Ekman layer which is referred to as Ekman pumping. Enhanced Ekman pumping around 5–10°N or °S leads to a weaker tropical cell with decreased upwelling at the equator and warmer SST. Again the Bjerknes feedback might amplify the equatorial effects. In summary

$$w_{y=0^o} \propto -w^{\nabla\times\boldsymbol{\tau}}_{y=10^o} \propto \nabla \times \boldsymbol{\tau}_{y=10^o}, \tag{7}$$

which cools SST at the equator. That is the effect observed in the Tiedtke model at $\beta = 0$. (For simplicity, we have not included explicitly a similar effect from the Southern Hemisphere tropical cell.)

In support of the proposed mechanism for the double ITCZ in Tiedtke, we inspect the wind response pattern difference between Nordeng and Tiedtke (Fig. 6 right panel), and note that the zonal gradient in the equator-ward flow between 5 to 10°N leads to stronger Ekman pumping in Nordeng at off-equatorial latitudes and reduced upwelling at the equator. This counteracts the effect of the increased easterlies at the equator. It is the balance between these two opposing effects which determines what will happen with the cold tongue at the equator when the momentum flux is varied between COSMOS-T ($\beta = 0$) and COSMOS-N ($\beta = 1$). When β is varied between 1 and 0, the magnitude of average meridional wind stress between 150°E and 150°W decreases from about -40 to about 0 (10^{-3} N/m^2, Fig. 8), assuming that the wind stress pattern is roughly fixed, this suggests that the associated wind stress curl increases as β goes from 1 to 0, decreasing the off-equatorial Ekman pumping with a cooling of the equatorial cold tongue as a result.

Coupled ocean-atmosphere interaction will modify the initial cooling effect from off-equatorial wind stress curl. In

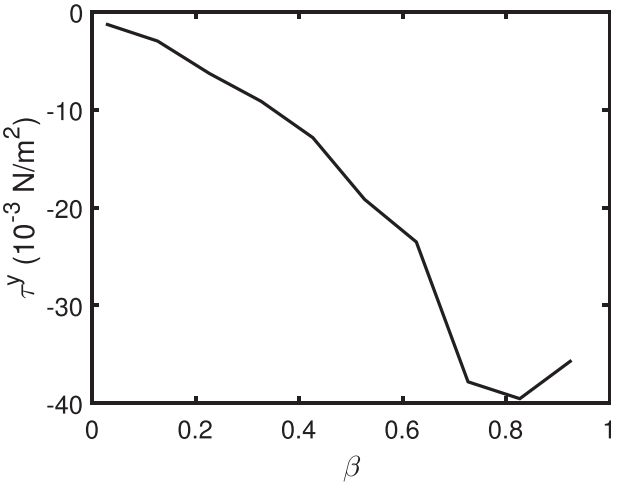

FIG. 8. Cross equatorial meridional wind at the central Pacific (150°E-150°W, 5°S-5°N). β changes from small value to close to 1 without changing the other two weights $(\alpha_o, \gamma_o) = (1.210, 0.682)$.

particular, the strong equatorial trade winds and cold tongue in COSMOS-T indicates that the positive Bjerknes feedback amplifies this negative tendency (Fig. 3).

For the above explanation of how opposite causes could have the same effect to make sense, we must also show that the two mechanisms do not combine linearly in the supermodel. We hypothesize that this is a consequence of the same nonlinearities in the atmosphere-ocean coupling that maintain ENSO. A principal nonlinearity comes from the dependence of the sub-thermocline temperature on thermocline depth, which in turn depends on upwelling velocity w.[49] Temperature change in eastern Pacific is thus implicitly nonlinear in w. The intrinsic contribution of the AGCMs contributions to equatorial upwelling, $w^{\tau^x}_{y=0^o}$, and off-equatorial upwelling, $w^{\nabla\times\tau}_{y=10^o}$, thus do not combine linearly in the supermodel, and the cold tongue effect at either extreme is more prevalent than it is in the middle, explaining the success of the supermodel. That is, the two contributions to w do not directly add since we do not imagine that they occur at the same longitudes, and the large cooling effects for Nordeng and Tiedtke separately do not average in the supermodel because of the nonlinear dependence on w.

C. The proposed mechanism in the nonlinear regime

Coupled ocean-atmosphere feedbacks make it difficult to detect the intrinsic differences between the two AGCMs in fully coupled simulations. These feedbacks also mean that the structure and strength of the simulated AGCM differences depend on the basic state of the climate model. This is because rainfall and wind patterns in the tropics are intimately linked to the underlying SST. Differences between the models are better represented by small perturbations to these patterns.

As further evidence for the proposed mechanism, we consider changes under a linear regime by perturbing only β close to the optimal value β_o without changing the other two weights $(\alpha_o, \gamma_o) = (1.210, 0.682)$. The change is sufficiently small that the response is to first order linear, and thus easier to understand. Figure 9 shows that the largest change is in the meridional winds, which alter the off-equatorial wind stress curl and lead to increase (decrease) $w^{\nabla\times\tau}_{y=10^o}$ as the momentum flux weight is slightly bigger (smaller). According to the above, this leads to suppressed (enhanced)

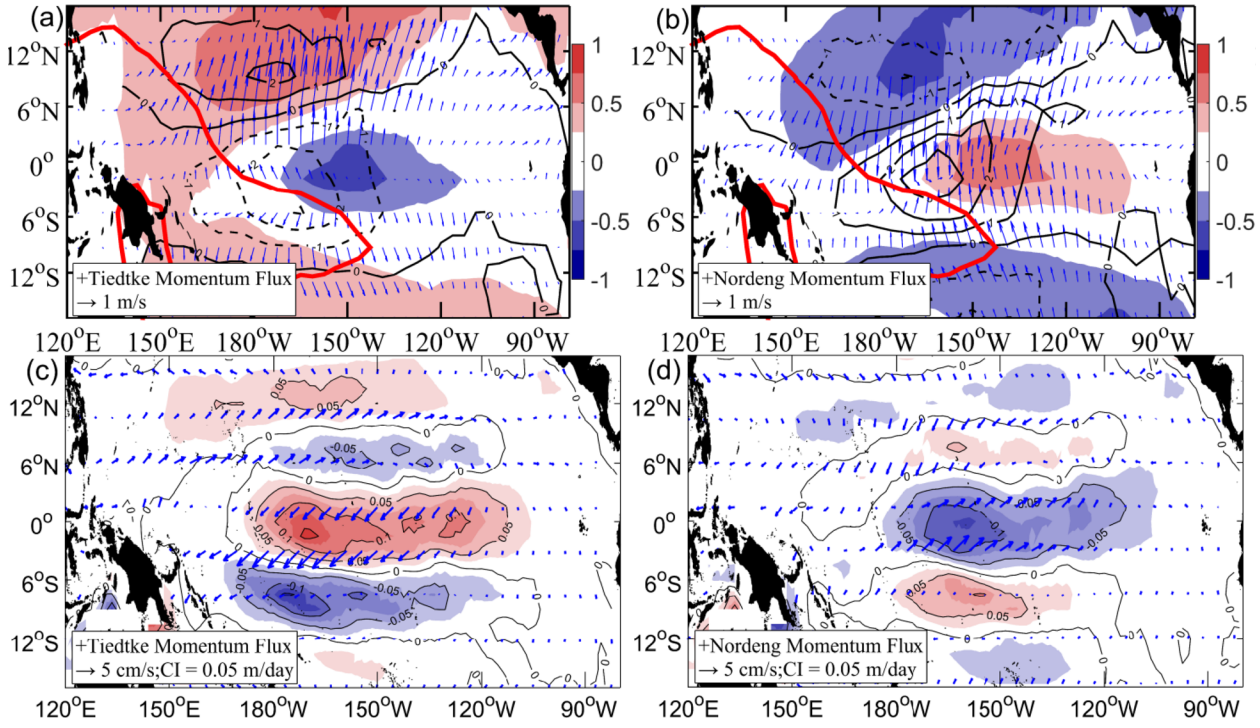

FIG. 9. Sensitivity to perturbations of the momentum flux (adapted from Fig. S4, Ref. 9). Here we present the anomaly of the perturbed cases (more flux from Nordeng atmosphere or from Tiedtke atmosphere) and SUMO: [(a) and (b)] SST (shading), precipitation (contours with interval 1 mm/day), and surface winds (vectors), with the SUMO warm pool enclosed by the bold red line (28.5 °C); [(c) and (d)] ocean upwelling speed at 50 m deep (shading) and averaged ocean surface (0–50 m) currents (vectors).

upwelling at the equator. The weaker (stronger) equatorial upwelling and the anomalous upwelling (downwelling) off the equator produce an anomalous meridional temperature differential in both hemispheres. While there may be a positive feedback with the SST anomalies acting to enhance the meridional wind changes, the positive Bjerknes feedback and nonlinear effects of upwelling appear of minor importance. Thus, we can see how differences in the off-equatorial meridional winds as isolated from strong-coupled feedbacks can lead to east-west shifts of the cold tongue.

A thought experiment provides some insight into the nonlinear regime. From the sign of changes in the perturbation experiment, we may anticipate that reducing β will lead to a westward expansion of the cold tongue leading to the double ITCZ state found in the Tiedtke model. We may also expect for the larger reduction in β that positive Bjerknes feedback will become active to strengthen the easterly zonal winds and cooling tendency. Likewise increasing β will lead to an eastward contraction of the cold tongue and an El Niño like state, as also seen in the phase diagram. Here we expect that the Bjerknes feedback will become active to strengthen the westerly zonal winds and warming tendency. These changes are consistent with wind stress curl changes induced by increasing cross equatorial winds as β varies from 0 to 1 (Fig. 8). However, as $\beta \to 1$ there is a bifurcation that is not as readily understood in the linear framework as the Nordeng model also exhibits a double ITCZ with a strong cold tongue (Fig. 3). Thus, another process must dominate as $\beta \to 1$. Our hypothesis is that this process is the intrinsic tendency for the Nordeng model to have stronger easterly trade winds. It appears to dominate as the Tiedtke effect weakens. Note it is difficult to verify this effect because of the coupled feedbacks linking atmospheric and oceanic states.

V. DIAGNOSING SUPERMODEL PHASE CHANGES

As described above, we propose that two main effects lead, respectively, to distinct contributions to equatorial upwelling, $w^{\tau^x}_{y=0^o}$, and off-equatorial upwelling, $w^{\nabla\times\boldsymbol{\tau}}_{y=0^o}(w^{\nabla\times\boldsymbol{\tau}}_{y=0^o} = -2w^{\nabla\times\boldsymbol{\tau}}_{y=10^o})$, imagined to occur at different longitudes, that combine nonlinearly to build up the climate state of the supermodel. A schematic diagram is used to explain the changes in the mean state for different strength of $w^{\tau^x}_{y=0^o}$ and $w^{\nabla\times\boldsymbol{\tau}}_{y=0^o}$ that correspond to transitions in the phase diagram. Figures 9(a) and 9(b) show that $w^{\nabla\times\boldsymbol{\tau}}_{y=0^o}$ contributes anomalous upwelling when β is smaller (approaching the full Tiedtke momentum state). This suggests that it is the $w^{\nabla\times\boldsymbol{\tau}}_{y=0^o}$ induced stronger upwelling in Tiedtke atmosphere that leads to excessive cold tongue in COSMOS-T. However, $w^{\nabla\times\boldsymbol{\tau}}_{y=0^o}$ becomes weaker or even downwelling as β becomes bigger (approaching to the full Nordeng momentum state), implying $w^{\nabla\times\boldsymbol{\tau}}_{y=0^o}$ is weak (Fig. 8) and the excessive cold tongue of COSMOS-N is mainly driven by the equatorial wind component, $w^{\tau^x}_{y=0^o}$. Here we only claim that one of these upwelling processes is the leading order effect in each constituent model. Based on this hypothesis, the nonlinear combination of these two effects can be categorized into the four different stages located on the phase diagram. Note that the combination of the two intrinsic atmospheric wind stresses initially modifies the mean SST distribution and that subsequently coupled atmosphere-ocean feedbacks further shape the climatological mean state.

The first stage [Fig. 10(a)] is when $w^{\nabla\times\boldsymbol{\tau}}_{y=0^o}$ contributes much stronger equatorial upwelling than $w^{\tau^x}_{y=0^o}$, so that an excessive cold tongue (blue line) is formed due to the strong upwelling. This is accompanied by downwelling off the equator. Both negative off-equator wind stress curl and equatorial easterly tend to increase equatorial upwelling. Note that the surface wind will adjust associated with the change of the SST structure as well. This stage can be regarded as the double ITCZ phase close to COSMOS-T.

The second stage [Fig. 10(b)] is when $w^{\nabla\times\boldsymbol{\tau}}_{y=0^o}$ contributes less equatorial upwelling than that in the first stage [Fig. 10(a)]. The cold tongue strength also becomes much smaller than it is in the first stage if the effect of the change of $w^{\tau^x}_{y=0^o}$ is smaller than that of the change of $w^{\nabla\times\boldsymbol{\tau}}_{y=0^o}$. Therefore the cold tongue no longer so extends excessively to the western Pacific. The western edge of the cold tongue sits close to the International Date Line. This stage can be regarded as the single ITCZ phase close to SUMO.

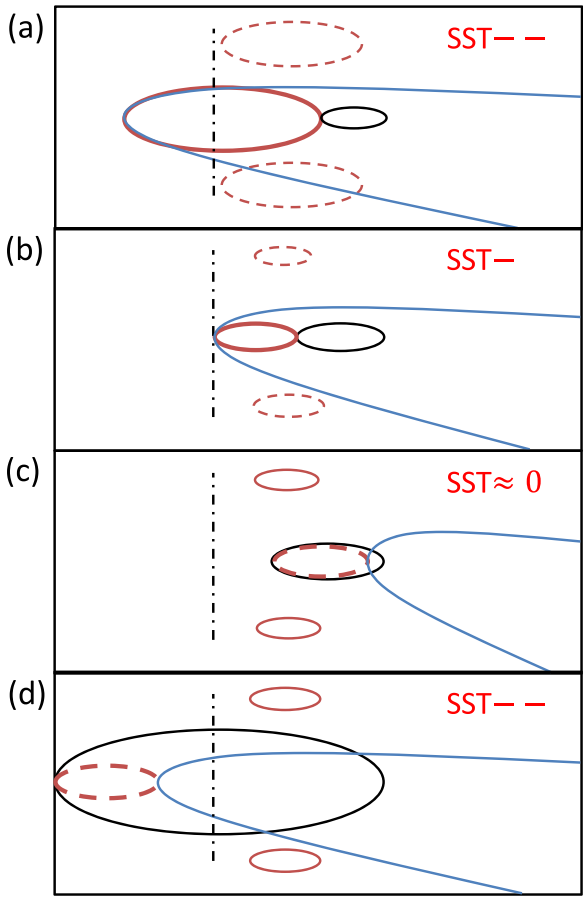

FIG. 10. Schematics of the interaction of the two intrinsic contributions, $w^{\nabla\times\boldsymbol{\tau}}$ (red circles) and $w^{\tau^x}_{y=0^o}$ (black circle). Solid circles indicate upwelling and dashed circles downwelling. Blue solid line indicates the cold tongue size and location associated with the changes of equatorial upwelling. The central line indicates the International Date Line which is regarded as a realistic boundary of the Pacific cold tongue. The four different panels present (a) double ITCZ phase close to COSMOS-T, (b) single ITCZ phase close to SUMO, (c) El Niño phase, and (d) single ITCZ phase close to COSMOS-N.

The third stage [Fig. 10(c)] is when $w^{\nabla\times\tau}_{y=0^o}$ contributes anomalous downwelling which compensates $w^{\tau^x}_{y=0^o}$ and leads to reduced equatorial upwelling and a more weakened cold tongue. This weakening of the equatorial SST gradient also weakens the SST-driven equatorial trade winds. This phase can be regarded as the El Niño phase. Also, the compensation of $w^{\nabla\times\tau}_{y=0^o}$ and $w^{\tau^x}_{y=0^o}$ build up an unstable balance that easily breaks down (as implied by the rapid transition in the phase diagram between El Niño and Nordeng double ITCZ phases).

The fourth stage [Fig. 10(d)] is when $w^{\tau^x}_{y=0^o}$ dominates the system with anomalous downwelling contributed by $w^{\nabla\times\tau}_{y=0^o}$. Therefore the cold tongue becomes larger and so does the part of the equatorial easterly that is a response to the increase of the equatorial SST gradient. The equatorial easterly is also stronger in this stage, since the SST-driven wind is much bigger in the Nordeng atmosphere. Thus the excessive cold tongue becomes the prevailing phenomenon in this stage. This stage can be regarded as the double ITCZ phase close to COSMOS-N.

We regard the cold tongue strength as the final footprint of the interaction of $w^{\tau^x}_{y=0^o}$ and $w^{\nabla\times\tau}_{y=0^o}$. It is related to other features in a complex way, based on the relationship of SST structure to surface winds and ocean circulation. For example, we claim that $w^{\tau^x}_{y=0^o}$ is increased from the second stage to the third stage. However, it is not surprising that the equatorial wind stress at the second stage is bigger than that at the third stage because the weakening of the cold tongue leads to an eastern extended Pacific warm pool. This weakens the equatorial SST gradient and the associated equatorial wind stress, regardless of the intrinsic difference in $w^{\tau^x}_{y=0^o}$ between the two AGCM's.

VI. DISCUSSION AND SUMMARY

Supermodeling offers to improve climate modeling, at little computational cost, by dynamically combining different models, each of which has been optimized in its own parameter space. The interactive ensemble version of supermodeling, which connects the different models only through their fluxes at the ocean-atmosphere interface, allows a broad range of basic model states to be simulated by changing only the heat flux weights and momentum flux weights and also has the potential to reduce model systematic error by optimizing those weights. Considering only heat and momentum fluxes, the basic state of the interactive models with intermediate values of the flux weights can be divided into three groups: double ITCZ, single northern ITCZ, and El Niño. These three states represent different physically possible tropical climate states that appear also as climate model mean biases, as aforementioned in Sec. II. To understand the supermodel's behavior, it is vital to understand how the states change in weight space.

The combination of wind-driven equatorial upwelling $w^{\tau^x}_{y=0^o}$ and off-equatorial upwelling $w^{\nabla\times\tau}_{y=10^o}$ play important roles in determining the interactive ensemble model states, with possible results as described in our conceptual analysis. Four difference possible stages are suggested here based on the combination of $w^{\tau^x}_{y=0^o}$ and $w^{\nabla\times\tau}_{y=10^o}$ and the associated total upwelling. In the double ITCZ phase, $w^{\nabla\times\tau}_{y=10^o}$ and $w^{\tau^x}_{y=0^o}$ contribute more equatorial upwelling in COSMOS-T and COSMOS-N, respectively. And the non-linear combination of the two effects can produce a model mean state close to the SUMO state or the single ITCZ phase, as well as a permanent El Niño state. With the proposed mechanism, it is seen that the non-linearities in the coupled ocean-atmosphere system, which are well known and are essential to the El Niño phenomenon, are also essential to the success of the supermodeling strategy as compared to *a posteriori* averaging of models outputs.

This study begins to answer the broader question of how constituent models exhibiting the same qualitative type of error, such as a double ITCZ, can dynamically combine in a supermodel to remove that error. Obviously, the error would remain in any weighted average of model outputs. It appears that a trained supermodel (here interactive ensemble) can capture features of a critical state, such as the single ITCZ state that exhibits ENSO transitions, that is typically missed by the separate constituent models. Where the criticality depends on interactions between phenomena at different scales, it is indeed not surprising that arbitrary parameterizations of sub-grid scale processes would fail to capture the requisite balances. Explorations with other types of supermodels formed from a variety of models, in climate science or elsewhere, are needed to test this interpretation of combining models dynamically.

ACKNOWLEDGMENTS

We thank two anonymous reviewers and the editor for their suggestions and for stimulating discussions amongst the authors that improved the manuscript. This study was supported by the ERC (Grant No. 648982) and Marie Sklodowska-Curie Actions–Individual Fellowship (MSCA-IF, Grant No. 658602). This work has also received a grant for computer time from the Norwegian Program for supercomputing (NOTUR, Project Nos. nn9207k, nn9039k, nn9385k) as well as storage space (NORSTORE, Project No. ns9207k). GPCP precipitation data were provided by the NOAA/OAR/ESRL PSD, Boulder, Colorado, USA, from their website at http://www.esrl.noaa.gov/psd.

[1]T. Reichler and J. Kim, Bull. Am. Meteorol. Soc. **89**(3), 303–311 (2008).
[2]L. M. Pecora, T. L. Carroll, G. A. Johnson, D. J. Mar, and J. F. Heagy, Chaos **7**(4), 520–543 (1997).
[3]G. S. Duane and J. J. Tribbia, Phys. Rev. Lett. **86**(19), 4298–4301 (2001).
[4]G. S. Duane and J. J. Tribbia, J. Atmos. Sci. **61**(17), 2149–2168 (2004).
[5]P. H. Hiemstra, N. Fujiwara, F. M. Selten, and J. Kurths, Nonlinear Processes Geophys. **19**(6), 611–621 (2012).
[6]F. Lunkeit, Chaos **11**(1), 47–51 (2001).
[7]L. A. van den Berge, F. M. Selten, W. Wiegerinck, and G. S. Duane, Earth Syst. Dyn. **2**(1), 161–177 (2011).
[8]G. S. Duane, M.-L. Shen, and N. S. Keenlyside, in International Symposium on Topical Problems of Nonlinear Wave Physics, Moscow-St. Petersburg, Russia (2017).
[9]M.-L. Shen, N. Keenlyside, F. Selten, W. Wiegerinck, and G. S. Duane, Geophys. Res. Lett. **43**(1), 359–366, https://doi.org/10.1002/2015GL066562 (2016).
[10]D. E. Waliser and N. E. Graham, J. Geophys. Res.: Atmos. **98**(D7), 12881–12893, https://doi.org/10.1029/93JD00872 (1993).
[11]E. Kalnay, M. Kanamitsu, R. Kistler, W. Collins, D. Deaven, L. Gandin, M. Iredell, S. Saha, G. White, J. Woollen, Y. Zhu, A. Leetmaa, R.

Reynolds, M. Chelliah, W. Ebisuzaki, W. Higgins, J. Janowiak, K. C. Mo, C. Ropelewski, J. Wang, R. Jenne, and D. Joseph, Bull. Am. Meteorol. Soc. **77**(3), 437–471 (1996).
[12]N. A. Rayner, D. E. Parker, E. B. Horton, C. K. Folland, L. V. Alexander, D. P. Rowell, E. C. Kent, and A. Kaplan, J. Geophys. Res.: Atmos. **108**(D14), 4407, https://doi.org/10.1029/2002JD002670 (2003).
[13]S. G. H. Philander, D. Gu, G. Lambert, T. Li, D. Halpern, N.-C. Lau, and R. C. Pacanowski, J. Clim. **9**(12), 2958–2972 (1996).
[14]S. A. Klein and D. L. Hartmann, J. Clim. **6**(8), 1587–1606 (1993).
[15]K.-M. Lau, H.-T. Wu, and S. Bony, J. Clim. **10**(3), 381–392 (1997).
[16]N. Hirota, Y. N. Takayabu, M. Watanabe, and M. Kimoto, J. Clim. **24**(18), 4859–4873 (2011).
[17]K. van der Wiel, A. J. Matthews, M. M. Joshi, and D. P. Stevens, Clim. Dyn. **46**(5), 1683–1698 (2016).
[18]S. M. Kang, I. M. Held, D. M. W. Frierson, and M. Zhao, J. Clim. **21**(14), 3521–3532 (2008).
[19]D. M. W. Frierson, Y.-T. Hwang, N. S. Fuckar, R. Seager, S. M. Kang, A. Donohoe, E. A. Maroon, X. Liu, and D. S. Battisti, Nat. Geosci. **6**(11), 940–944 (2013).
[20]J. D. Neelin, M. Latif, M. A. F. Allaart, M. A. Cane, U. Cubasch, W. L. Gates, P. R. Gent, M. Ghil, C. Gordon, N. C. Lau, C. R. Mechoso, G. A. Meehl, J. M. Oberhuber, S. G. H. Philander, P. S. Schopf, K. R. Sperber, K. R. Sterl, T. Tokioka, J. Tribbia, and S. E. Zebiak, Clim. Dyn. **7**(2), 73–104 (1992).
[21]C. R. Mechoso, A. W. Robertson, N. Barth, M. K. Davey, P. Delecluse, P. R. Gent, S. Ineson, B. Kirtman, M. Latif, H. L. Treut, T. Nagai, J. D. Neelin, S. G. H. Philander, J. Polcher, P. S. Schopf, T. Stockdale, M. J. Suarez, L. Terray, O. Thual, and J. J. Tribbia, Mon. Weather Rev. **123**(9), 2825–2838 (1995).
[22]H. Bellenger, E. Guilyardi, J. Leloup, M. Lengaigne, and J. Vialard, Clim. Dyn. **42**(7–8), 1999–2018 (2014).
[23]J. Lloyd, E. Guilyardi, and H. Weller, Clim. Dyn. **37**(7–8), 1271–1292 (2011).
[24]C.-C. Ma, C. R. Mechoso, A. W. Robertson, and A. Arakawa, J. Clim. **9**(7), 1635–1645 (1996).
[25]C. R. Mechoso, T. Losada, S. Koseki, E. Mohino-Harris, N. Keenlyside, A. Castaño-Tierno, T. A. Myers, B. Rodriguez-Fonseca, and T. Toniazzo, Geophys. Res. Lett. **43**(20), 11057, https://doi.org/10.1002/2016GL071150 (2016).
[26]Y.-T. Hwang and D. M. W. Frierson, Proc. Natl. Acad. Sci. U.S.A. **110**(13), 4935–4940 (2013).
[27]X. Zhang, W. Lin, and M. Zhang, J. Geophys. Res.: Atmos. **112**(D12), D12102, https://doi.org/10.1029/2006JD007878 (2007).
[28]G. Li and S.-P. Xie, J. Clim. **27**(4), 1765–1780 (2014).
[29]F.-F. Jin, J. Atmos. Sci. **54**(7), 811–829 (1997).
[30]D. Gu and S. G. H. Philander, Science **275**(5301), 805–807 (1997).
[31]R. Kleeman, J. P. McCreary, and B. A. Klinger, Geophys. Res. Lett. **26**(12), 1743–1746, https://doi.org/10.1029/1999GL900352 (1999).
[32]Z. Liu, J. Phys. Oceanogr. **24**(6), 1153–1165 (1994).
[33]J. P. McCreary and P. Lu, J. Phys. Oceanogr. **24**(2), 466–497 (1994).
[34]P. Lu, J. P. McCreary, and B. A. Klinger, J. Phys. Oceanogr. **28**(1), 62–84 (1998).
[35]R. C. Perez and W. S. Kessler, J. Phys. Oceanogr. **39**(1), 27–49 (2009).
[36]D. Matei, N. Keenlyside, M. Latif, and J. Jungclaus, J. Clim. **21**(18), 4691–4709 (2008).
[37]N. J. Burls, L. Muir, E. M. Vincent, and A. Fedorov, Clim. Dyn. **49**(5–6), 2093–2113 (2016).
[38]B. P. Kirtman and J. Shukla, Geophys. Res. Lett. **29**(10), 1367 (2002).
[39]B. P. Kirtman, D. Min, P. S. Schopf, and E. K. Schneider, COLA Technical Reports (2013), avaialable at http://www.m.monsoondata.org/pubs/tech.html and ftp://cola.gmu.edu/pub/ctr/ctr_154.pdf.
[40]J. H. Jungclaus, N. Keenlyside, M. Botzet, H. Haak, J. J. Luo, M. Latif, J. Marotzke, U. Mikolajewicz, and E. Roeckner, J. Clim. **19**(16), 3952–3972 (2006).
[41]E. Roeckner, G. Bäuml, L. Bonaventura, R. Brokopf, M. Esch, M. Giorgetta, S. Hagemann, I. Kirchner, L. Kornblueh, E. Manzini, A. Rhodin, U. Schlese, U. Schulzweida, and A. Tompkins, Report No. 349, 2003.
[42]S. J. Marsland, H. Haak, J. H. Jungclaus, M. Latif, and F. Röske, Ocean Modell. **5**(2), 91–127 (2003).
[43]S. Valcke, Geosci. Model Dev. **6**(2), 373–388 (2013).
[44]T.-E. Nordeng, ECMWF Technical Report, No. 206 (Shinfield Park, Reading, UK, 1994), 41 pp., avaialable at https://www.ecmwf.int/sites/default/files/elibrary/1994/11393-extended-versions-convective-parametrization-scheme-ecmwf-and-their-impact-mean-and-transient.pdf (1994).
[45]M. Tiedtke, Mon. Weather Rev. **117**(8), 1779–1800 (1989).
[46]B. Möbis and B. Stevens, J. Adv. Model. Earth Syst. **4**(4), M00A04 (2012).
[47]J. A. Nelder and R. Mead, Comput. J. **7**(4), 308–313 (1965).
[48]F. F. Jin, J. Atmos. Sci. **55**(14), 2458–2469 (1998).
[49]S. E. Zebiak and M. A. Cane, Mon. Weather Rev. **115**(10), 2262–2278 (1987).